ACS APPLIED ENERGY MATERIALS

www.acsaem.org Article

Hydrochloric Acid-Assisted Synthesis of Highly Dispersed MoS_2 Nanoflowers as the Cathode Material for Mg-Li Batteries

Zhennan Xiong, Guilei Zhu, Hui Wu, Gejun Shi, Pu Xu, Huimin Yi, Yiyang Mao, Baofeng Wang,* and Xuebin Yu*

Cite This: *ACS Appl. Energy Mater.* 2022, 5, 6274–6281 Read Online

ACCESS | Metrics & More | Article Recommendations | Supporting Information

ABSTRACT: The layered material MoS_2 has significant potential as a cathode material for hybrid Mg^{2+}/Li^+ batteries (MLIBs) due to its fast two-dimensional ion diffusion channel. However, the low capacity and poor cycling stability limit the practical application of MoS_2. Herein, highly dispersed MoS_2 nanoflowers with a large Brunauer–Emmett–Teller (BET) area of 118.25 $m^2\ g^{-1}$ and a large lattice spacing of 0.65 nm are synthesized by a one-step hydrothermal method. The obtained MoS_2 nanoflowers deliver a remarkable reversible capacity of 321 mA h g^{-1} at 0.1 A g^{-1}. Notably, it displays an impressive cycling stability with a reversible capacity of 103 mA h g^{-1} over 600 consecutive cycles at 1 A g^{-1}. The favorable electrochemical properties of the MoS_2 are attributed to the large BET area and increased lattice spacing that are more conducive to the full contact between the electrolyte and the material, thus promoting the diffusion of ions and improving the reaction kinetics. The results of the present study offer an idea to prepare highly dispersed MoS_2 with enhanced capacity and durability.

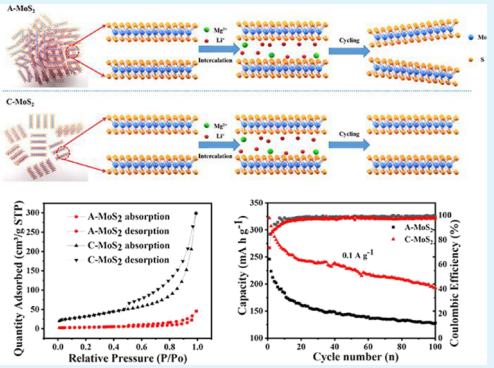

KEYWORDS: *hybrid Mg^{2+}/Li^+ batteries, MoS_2, nanoflowers, surface area, reaction kinetics*

1. INTRODUCTION

Lithium-ion batteries (LIBs) have attracted wide attention due to its high gravimetric energy density, high theoretical capacity, and long-term cycling durability.[1−3] However, the shortage of lithium resources and the defect of lithium dendrite growth on the anode surface restrict its practical applications.[4,5] Considering this case, magnesium-ion batteries (MIBs) have aroused wide interest due to the resource abundance and dendrite-free growth on the magnesium anode.[6] Besides, MIBs have a volumetric capacity of 3833 mA h cm^{-3} and a gravimetric capacity of 2205 mA h g^{-1} as Mg^{2+} transfers more electrons.[7,8] However, some grand challenges need to be overcome in order to promote the development of MIBs.[9] The slow diffusion kinetics can lead to a high polarization during charge–discharge processes.[10] To resolve this obstacle, MLIBs with a dual salt electrolyte were designed.[11] The system of hybrid battery comprises the Mg metal as the anode, Mg^{2+}/Li^+ dual salt as the electrolyte, and intercalated materials as cathodes, which can not only take full advantage of the merit of dendrite-free Mg anode, but also realize the rapid kinetic of Li^+ in the cathode materials.[12,13] To date, most reported MLIBs are Daniell-type cells, where only Li^+ is de-intercalated/intercalated from the cathode materials during charge–discharge process, and the energy density of the battery inevitably depends on the lithium salt solubility in the electrolyte.[14−17] However, the solubility of lithium salt in the solvent limits the energy density of MLBs in practice.[6] If the cathode materials can accommodate both Li^+ and Mg^{2+}, the MLIBs will avoid the disadvantages of Daniell-type cells and display a high energy density.[18] Therefore, it is necessary to search for suitable cathode materials to accommodate Mg^{2+}/Li^+.

MX_2 (M = Ti, V, Mo, and W; X = S and Se) have been considered as promising cathode materials for MIBs because they can greatly improve the transport of Mg^{2+} through the unique two-dimensional structure.[19−22] Molybdenum disulfide (MoS_2), as one typical member of the most classical transition-metal dichalcogenides, has attracted wide concern as the cathode of MLIBs.[23,24] Although bulk MoS_2 is not conducive to Mg^{2+} intercalation, the exfoliated MoS_2 is more favorable to the diffusion and storage of Mg^{2+}.[25,26] For example, Chang's group reported the Li intercalation-exfoliated MoS_2, which optimized the microstructure of MoS_2 for easier intercalation of various ions.[5] Furthermore, Jiao and co-workers prepared exfoliated three-dimensional (3D) porous MoS_2 and enlarged the interlayer spacing by intercalating graphene into MoS_2. The flexible electrode showed an initial specific capacity of

Received: February 28, 2022
Accepted: April 21, 2022
Published: May 3, 2022

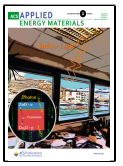

https://doi.org/10.1021/acsaem.2c00611
ACS Appl. Energy Mater. 2022, 5, 6274–6281

115.9 mA h g^{-1} at 0.1 A g^{-1} and high reversible specific capacity of 82.5 mA h g^{-1} over 50 cycles, which is largely improved compared with bulk MoS_2.[27] Although there are many reports on the synthesis of dispersed MoS_2, such as mechanical exfoliation,[28] electrochemical exfoliation,[27] and liquid exfoliation,[29] these methods normally involve complicated synthesis steps or are time- and energy-consuming. Therefore, seeking a simple method to synthesize highly dispersed nano-MoS_2 is of great significance for its application.

In this work, nanostructured MoS_2 with different dispersion degrees was synthesized using hydrochloric acid to control the concentration of sulfur ions in the solution. When the pH of the solution was adjusted to 0.9, the highly dispersed MoS_2 nanoflowers with a large Brunauer−Emmett−Teller (BET) area of 118.25 m^2 g^{-1} and large lattice spacing of 0.65 nm are obtained. The dispersed morphology and increased lattice spacing are more conducive to the full contact between electrolyte and material and shorten the ion diffusion path distance in the electrode, which promotes the diffusion of ions and improves the reaction kinetics. As a result, the MoS_2 delivers high initial discharge capacities (321.9 and 200.6 mA h g^{-1} at 0.1 and 1 A g^{-1}, respectively) and excellent cycling performance (192.8 mA h g^{-1} over 100 consecutive cycles at 0.1 A g^{-1} and 102.8 mA h g^{-1} over 600 consecutive cycles at 1 A g^{-1}, respectively).

2. EXPERIMENTAL SECTION

2.1. Synthesis of MoS_2. The raw materials used in the experiment were all analytically pure and were used without further purification. The MoS_2 with different morphologies were synthesized by a one-step hydrothermal reaction using ammonium molybdate tetrahydrate ($H_{24}Mo_7N_6O_{24}{\cdot}4H_2O$) and thiourea ($CH_4N_2S$) as raw materials, and hydrochloric acid (HCl) was used as a pH regulator of the solution. In a typical synthesis, 1 mM (1.2359 g) $H_{24}Mo_7N_6O_{24}{\cdot}4H_2O$ and 15 mM (1.1989 g) CH_4N_2S were dissolved in a 60 mL solution with the pH of 7. After stirring for 30 min, it was transferred into a 100 mL Teflon-lined stainless autoclave and kept at 220 °C for 18 h. Then, the obtained product needs to be centrifuged three times with ethanol and deionized water, and the A-MoS_2 sample could be obtained after drying in vacuum kept at 60 °C for 12 h. B-MoS_2, C-MoS_2, and D-MoS_2 were fabricated when the pH of the solution was 4, 0.9, and 0.6, respectively.

2.2. Materials Characterizations. The as-prepared materials were tested by X-ray diffraction (XRD, Rigaku D/max 2000 diffractometer). The chemical state and element valence of the C-MoS_2 were measured by X-ray photoelectron spectroscopy (XPS, Thermo Scientific K-Alpha$^+$). The morphology was obtained by field-emission scanning electron microscopy (FE-SEM-4800-1, Japan). The microstructure analysis [(transmission electron microscopy (TEM), high-resolution TEM (HR-TEM), and selected area electron diffraction (SAED)] was carried out on the Thermo Fischer Talos F200x. The specific surface area of MoS_2 was recorded by the BET (Tristar II 3020 Version 3.02). Raman spectra of MoS_2 were characterized by the excitation wavelength of 532 nm (XploRA, France).

2.3. Electrochemical Measurements. The electrochemical performance of MoS_2 was characterized by using CR2032 coin cells. The active materials (70 wt %), conductive agent (20 wt %), and binder (10 wt %) were mixed to make a homogeneous slurry. The slurry was coated on stainless steel. The working electrode was obtained after drying at 80 °C for 12 h. The counter electrode and separator are magnesium metal and glass fiber, respectively. The APC electrolyte was synthesized using the method reported by Oren Mizrahi et al.[30] 0.25 M aluminum chloride ($AlCl_3$) was added to 7.5 mL of tetrahydrofuran to form a mixed solution, and then 2.5 mL of phenyl magnesium chloride (MgPhCl) was added. It was magnetically stirred for 24 h, and then lithium chloride (LiCl) of 0.01 M was added and stirred for 24 h to form the 1 M LiCl/0.25 M APC electrolyte. The whole process was carried out in a glovebox filled with argon gas. The galvanostatic charge and discharge (GCD) test was carried out on the NETWARE BTS-5 V battery test system. Cyclic voltammetry (CV) was carried out on the electrochemical workstation at a scanning rate of 0.1 mV s^{-1}. The electrochemical impedance spectroscopy (EIS) test (frequency from 10^{-2} to 10^5 Hz with voltage amplitude 5 mV) was conducted with an electrochemical workstation.

3. RESULTS AND DISCUSSION

The major steps involved in the synthesis are presented in Figure 1a. The chemical reaction equation of MoS_2 can be described as follows:[31,32]

$$CH_4N_2S + H_2O \rightarrow S^{2-} + CH_2N_2 + H^+ \quad (1)$$

$$MoO_4^{2-} + S^{2-} \rightarrow MoS_2 + SO_4^{2-} \quad (2)$$

$$H^+ + S^{2-} \leftrightarrow HS^- \quad (3)$$

$$HS^- + H^+ \leftrightarrow H_2S \quad (4)$$

As shown in formulas 1 and 2, CH_4N_2S hydrolyzes in solution to produce S^{2-} and MoS_2 is synthesized by the reaction of S^{2-} and MoO_4^{2-}. The formulas 3 and 4 indicate that sulfur ions are consumed by electrolysis in the solution. The sulfur concentration is the key parameter that controls the prospects of the material growth.[33]

When the concentration of H^+ was increased, the concentration of S^{2-} would also change, thus affecting the morphologies of MoS_2. Figure 1b−e shows the variations in MoS_2 by adjusting the pH value of the solution. As shown in Figure 1b and c, A-MoS_2 and B-MoS_2 show that the bulk structure is composed of nanosheets. For C-MoS_2, a unique nanoflower structure formed with highly dispersed nanosheets is observed as shown in Figure 1d. D-MoS_2 (Figure 1e) is also composed of nanosheets but tends to aggregate (Figure 1d). Clearly, MoS_2 nanosheets with different dispersion degrees can be synthesized by controlling the concentration of S^{2-} to affect the synthesis rate of MoS_2. The unique structure of highly dispersed nanosheets for C-MoS_2 is more conducive to the full contact between electrolyte and material and shortens the ion diffusion path distance in the electrode, which promotes the diffusion of ions and improves the reaction kinetics.

The as-prepared MoS_2 was characterized by XRD (Figure 2a). All diffraction peaks of the as-prepared MoS_2 index accurately to the MoS_2 with hexagonal structure (PDF#75-1539). Compared with the A-MoS_2, however, the peaks of B-MoS_2/C-MoS_2/D-MoS_2 at the (002) plane shift to a low angle. For example, the diffraction peaks of A-MoS_2 and C-MoS_2 at the (002) plane are observed around 14.3 and 13.7°, respectively. The shift of the diffraction peak indicates an increased interlay distance from 0.62 nm (A-MoS_2) to 0.65 nm (C-MoS_2), according to Bragg's formula.[26] The increase in lattice spacing should be ascribed to the intercalation of NH_4^+ and the formation of lattice oxygen in the MoS_2 layers during the hydrothermal process.[34,35] The Raman spectra in Figure 2b further present the structure of A-MoS_2 and C-MoS_2, in which the characteristic peaks observed around 380.2/382.1 and 406.7/406.6 cm^{-1} are corresponding to E^1_{2g} and A_{1g} Raman modes, respectively. The phenomenon of the peak shift is mainly attributed to the fact that the interlayer expansion results in a decrease in the interlaminar van der Waals force, which leads to a stronger out-of-plane vibration.[36,37] Figure 2c shows the N_2 adsorption/desorption isotherm of the as-

https://doi.org/10.1021/acsaem.2c00611
ACS Appl. Energy Mater. 2022, 5, 6274−6281

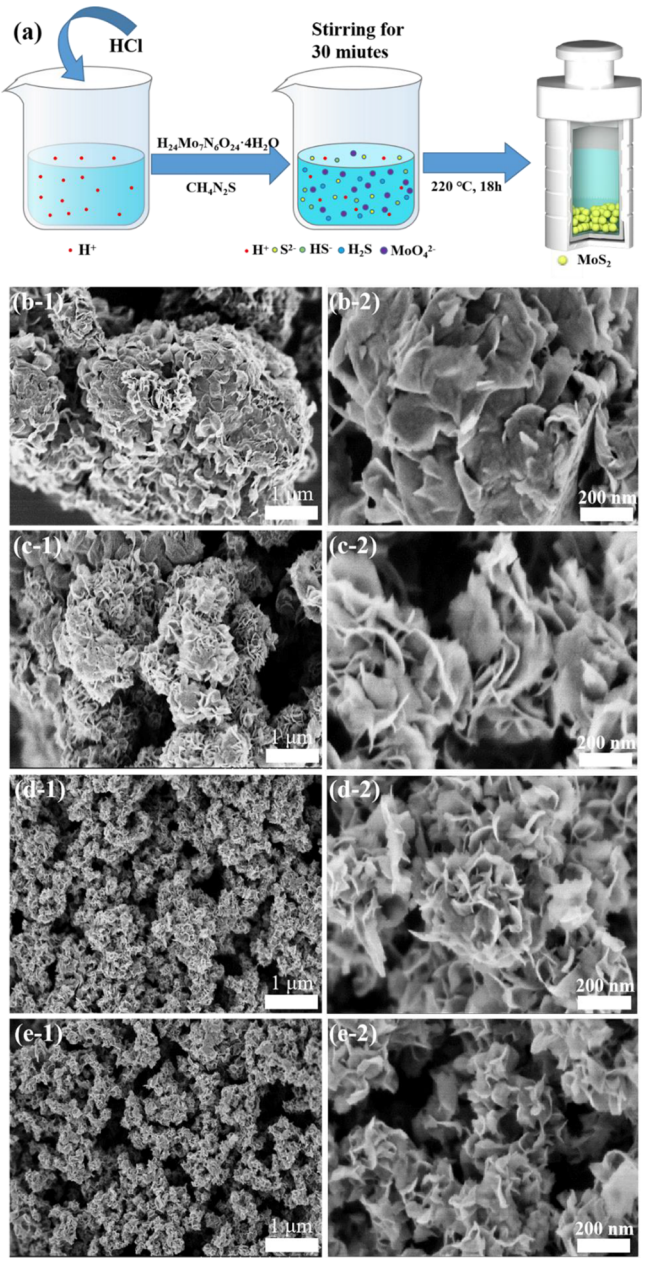

Figure 1. (a) Schematic illustration of the synthesis process of MoS_2. SEM images of (b) A-MoS_2, (c) B-MoS_2, (d) C-MoS_2, and (e) D-MoS_2.

prepared MoS_2 materials. A-MoS_2, B-MoS_2, and D-MoS_2 possess a BET area of 13.27, 18.75, and 102.32 m^2 g^{-1}, respectively, while the C-MoS_2 possesses a larger BET area of 118.25 m^2 g^{-1}. It can be seen that there are more abundant interconnected nanostructures in C-MoS_2. XPS was used to investigate the chemical states of Mo and S in the samples with the C-MoS_2, as shown in Figures 2d,e and S1, which indicates the presence of C, O, Mo, and S elements. Figure 2d shows that there are three main characteristic peaks in the spectra of Mo 3d. The peak with a binding energy of 226.9 eV belongs to S 2s, and the other two peaks with binding energies of 229.8 and 233.0 eV are indexed to Mo $3d_{5/2}$ and Mo $3d_{3/2}$ of Mo^{4+}, respectively.[38] The characteristic peaks of 162.6 and 163.8 eV displayed in Figure 2e are indexed to S $2P_{3/2}$ and S $2P_{1/2}$, respectively.[39]

The TEM images of A-MoS_2 show that the material is seriously stacked (Figure 2f), whereas C-MoS_2 has the feature of thin nanosheets in Figure 2g. The highly dispersed morphology of C-MoS_2 affirmed by TEM fits well with the results of SEM and BET. The abovementioned results indicate that by controlling the pH, two-dimensional MoS_2 nanosheets with the larger BET area were successfully synthesized. The HR-TEM images reveal that the interlayer spacing of A-MoS_2 is 0.62 nm, whereas the interlayer distance of C-MoS_2 expands to 0.65 nm (Figure 2h and i), consistent with the XRD results. The uniform distribution of Mo, S, and O elements in the materials could be seen from SEM energy-dispersive mapping images (Figure S2). The presence of the O element evidences the formation of lattice oxygen in the sample.[34,35] The SAED pattern demonstrates the polycrystalline structure for the C-MoS_2 material (Figure S3). Clearly, the C-MoS_2 material with a larger exposed surface area and interlayer spacing is beneficial to the full contact between electrolyte and material.

The CR2032-type coin cells were assembled to evaluate the electrochemical performance. The redox peaks of the initial three CV curves of C-MoS_2 are around 1.2 and 0.6 V, corresponding to the Mg^{2+}/Li^+ extraction and insertion behavior (Figure 3a). At current densities of 0.1, 0.5, 1, 2, 5, and 10 A g^{-1}, the C-MoS_2 electrode possesses high reversible capacities of 321.2, 218.9, 169.2, 137.3, 105.6, and 80.6 mA h g^{-1} (Figure 3b and c). For comparison, A-MoS_2 shows reversible capacities of 261.3, 149.8, 121.4, 93.9, 51.4, and 19.4 mA h g^{-1}. Obviously, the C-MoS_2 electrode displays impressive rate performance and higher reversible capacities. The B-MoS_2 and D-MoS_2 electrodes also achieve superior rate ability compared to the A-MoS_2 electrode, indicating that the high dispersion and expanded lattice spacing dominate the electrochemical performance of the MoS_2 electrode (Figure S4).

The cycle stability of MoS_2 was tested. The C-MoS_2 and A-MoS_2 electrodes deliver initial specific capacities of 321.9 and 245.9 mA h g^{-1} at 0.1A g^{-1} (Figure 3d). C-MoS_2 can maintain a specific capacity of 192.8 mA h g^{-1} after 100 cycles, while the capacity of A-MoS_2 decays to 128.1 mA h g^{-1}. Similarly, the discharge capacity of B-MoS_2/D-MoS_2 is also higher than that of A-MoS_2 (Figure S5), giving the same tendency as observed in rate performance. Figure S6 shows the GCD data of A-MoS_2 and C-MoS_2 cathodes at 0.1 A g^{-1}. The long cycling performance of A-MoS_2 and C-MoS_2 at 1 A g^{-1} is measured as shown in Figure 3e. It presents that the capacity of A-MoS_2 decreased to 70.1 mA h g^{-1} over 600 cycles, which shows poor reversible stability. As for C-MoS_2, the reversible capacity is 103 mA h g^{-1} over 600 cycles, showing excellent stability. We test the electrochemical performance of MoS_2 nanoflowers in pure Li^+ electrolyte and pure Mg^{2+} electrolyte and compare it with the properties in the Mg^{2+}/Li^+ electrolyte. The Mg^{2+}/Li^+, pure Li^+, and pure Mg^{2+} electrolytes deliver initial discharge capacities of 321.9, 30.5, and 39.3 mA h g^{-1}, respectively. The Mg^{2+}/Li^+ electrolyte can maintain a specific capacity of 244.25 mA h g^{-1} over 20 cycles, while that of pure Li^+ and pure Mg^{2+} electrolyte decays to 11.2 and 36.9 mA h g^{-1}. The favorable cycle performance can be obtained in the Mg^{2+}/Li^+ electrolyte (Figure S7). In addition, the cycle performance of the MoS_2 host reported in the literatures was collected and compared with C-MoS_2 (Table S1). Clearly, C-MoS_2 as the cathode material for MLBs shows a better electrochemical performance. The high capacity of the C-MoS_2 derives from the large BET area and large lattice spacing, which are conducive to the

https://doi.org/10.1021/acsaem.2c00611
ACS Appl. Energy Mater. 2022, 5, 6274−6281

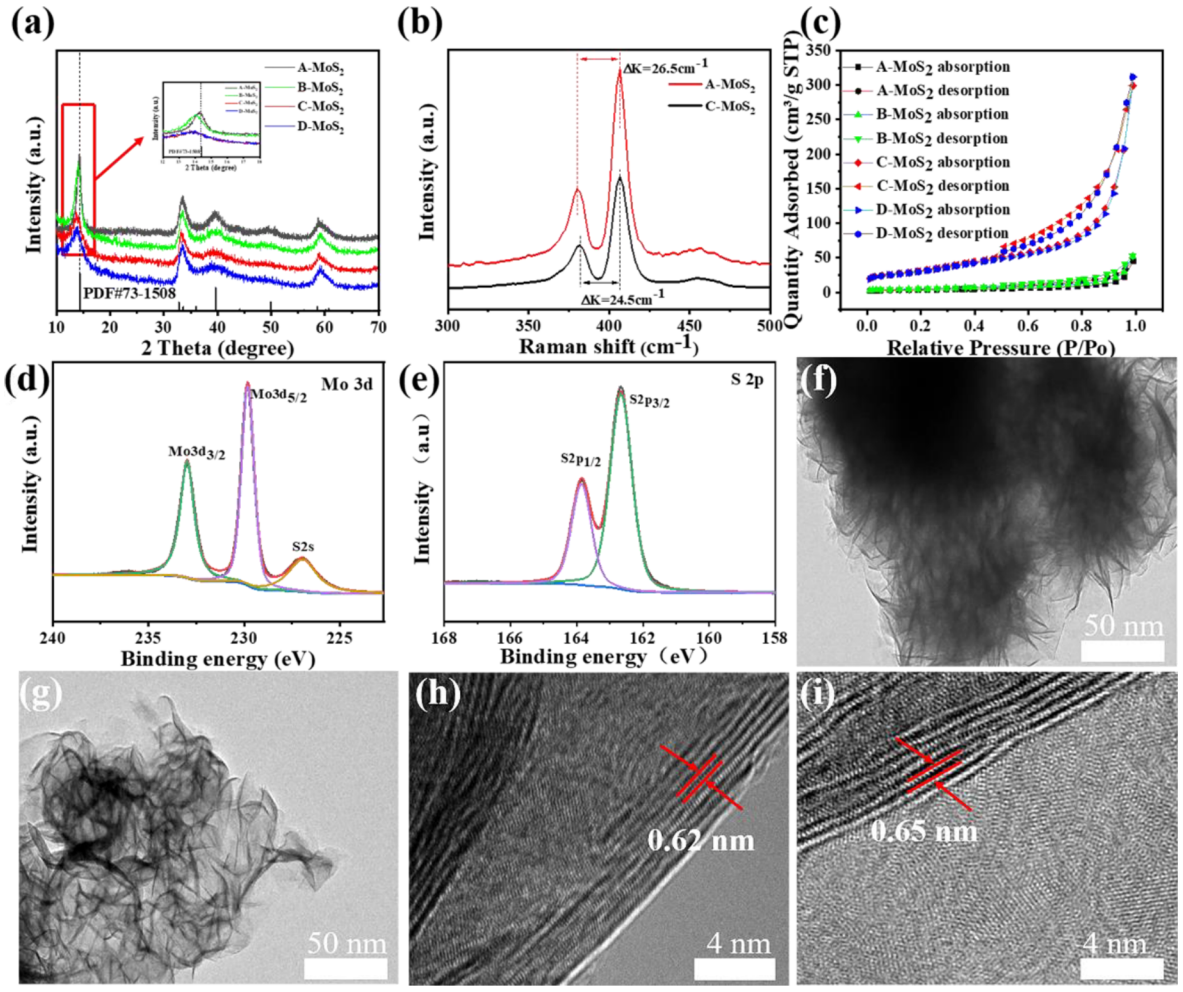

Figure 2. (a) XRD patterns of the as-prepared MoS_2 materials (the inset in the image shows the 12−18° range of MoS_2 materials). (b) Raman spectra of A-MoS_2 and C-MoS_2. (c) Nitrogen adsorption/desorption isotherm of the as-prepared MoS_2. XPS spectra of the C-MoS_2: (d) Mo 3d and (e) S 2p. (f, g) TEM and (h, i) HR-TEM images of A-MoS_2 and C-MoS_2.

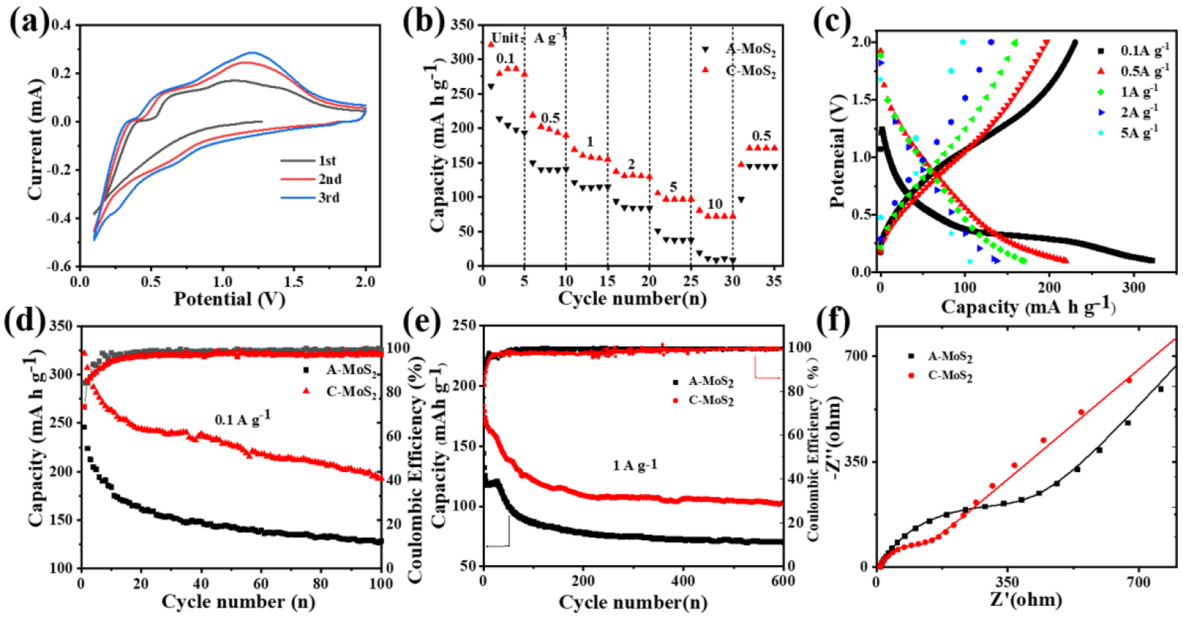

Figure 3. (a) CV profiles at 0.1 mV s^{-1} of C-MoS_2. (b) Rate capability at 0.1−10 A g^{-1} of A-MoS_2 and C-MoS_2. (c) Galvanotactic charge/discharge curves of C-MoS_2 batteries at various current densities. (d) Cycling performances of A-MoS_2 and C-MoS_2 at 0.1 A g^{-1}. (e) Long-term cycling stability at 1 A g^{-1} of A-MoS_2 and C-MoS_2. (f) Nyquist plots of A-MoS_2 and C-MoS_2.

https://doi.org/10.1021/acsaem.2c00611
ACS Appl. Energy Mater. 2022, 5, 6274−6281

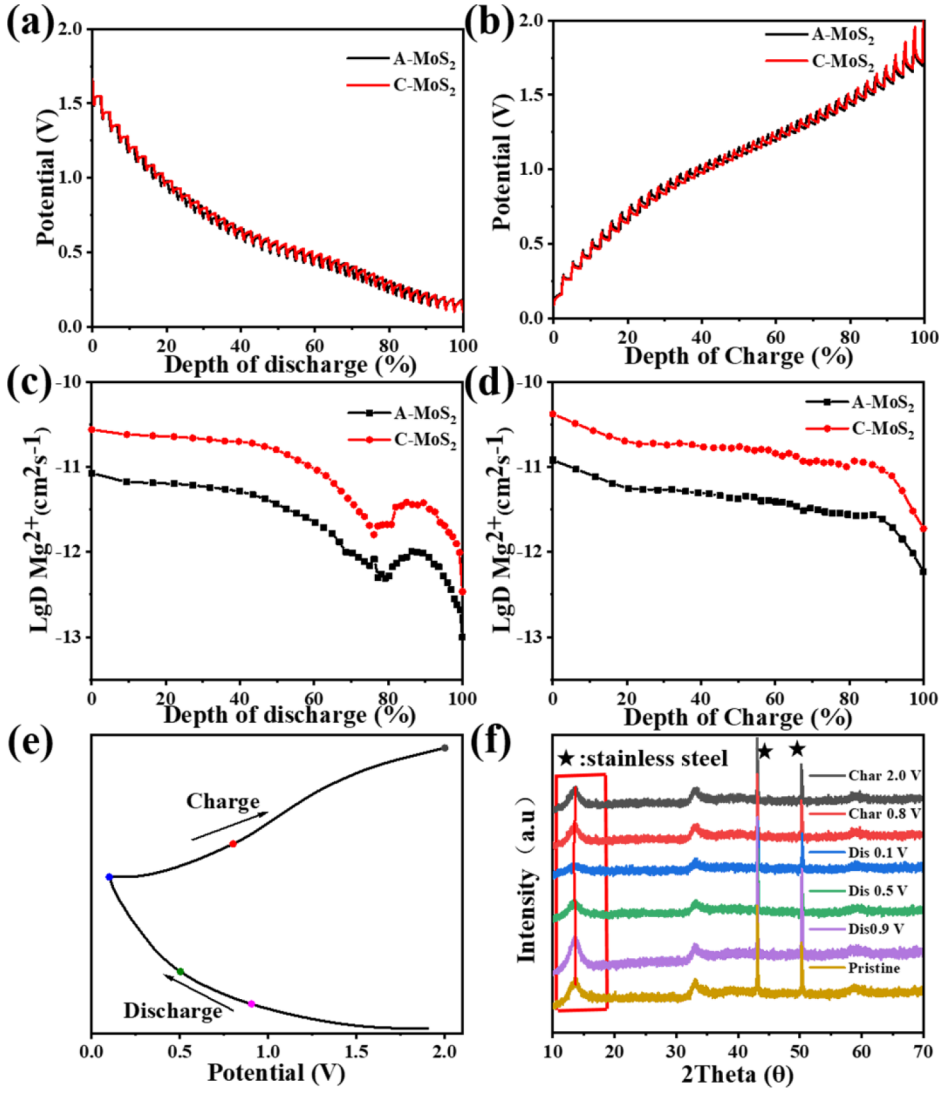

Figure 4. (a, b) GITT curves of A-MoS_2 and C-MoS_2 electrodes. (c, d) Mg^{2+} diffusion coefficient of A-MoS_2 and C-MoS_2 electrodes calculated via GITT curves in the discharged/charged state. (e) Galvanostatic charge and discharge curve of the C-MoS_2 cathode at the second cycle. (f) Ex situ XRD patterns of the C-MoS_2 electrode during the first cycle.

full contact between electrolyte and the material, and shortens the ion diffusion path distance in the electrode. In addition, EIS during the first cycling is carried out to investigate the reaction kinetics of C-MoS_2 and A-MoS_2, and the corresponding Nyquist plots are given in Figure 3f. The Nyquist plots consist of a semicircle at high frequencies and a slash at low frequencies. The semicircle corresponds to charge transfer resistance (R_{ct}), and the slash represents the Warburg impedance (Z_w) related to the Mg-Li ion diffusion.[40] We have fitted the Nyquist plots, and Figure S8 shows the equivalent circuit diagram. The R_{ct} values of C-MoS_2 and A-MoS_2 are 64.5 and 324.3 Ω, respectively, indicating that C-MoS_2 possesses much lower charge transfer resistance.

To evaluate the effect of interlayer distance and morphology on the diffusivity of ions in MoS_2, the galvanostatic intermittent titration technique (GITT) was employed to probe the diffusivity of ions.[41] Figure 4a and b shows the GITT curves of A-MoS_2 and C-MoS_2. The ion diffusivity D_{GITT} can be obtained via the formula:[42,43]

$$D_{GITT} = \frac{4}{\pi\tau}\left(\frac{m_B V_M}{M_B S}\right)^2\left(\frac{\Delta E_s}{\Delta E_t}\right)^2 \quad (5)$$

where τ, m_B, M_B, V_M, S, ΔE_t, and ΔE_s correspond to the relaxation time, the mass of active material, molar weight, molar volume, geometric area of the electrode, potential change caused by pulse and constant current charging/discharge, respectively. The calculated diffusion coefficient values of the C-MoS_2 are higher than that of A-MoS_2 (Figure 4c and d), which can be ascribed to the larger layer spacing and the dispersed two-dimensional MoS_2 nanosheets with a larger BET area, which are more conducive to ion transport. To learn the energy storage mechanism of the C-MoS_2 cathode in MLBs, ex situ XPS and ex situ XRD were carried out. Figure S9a and b shows the ex situ XPS spectra of the C-MoS_2 cathode measured at discharge and charge stages. When discharged to 0.1 V, the characteristic peaks of Li 1s and Mg 2p would appear. The characteristic peaks of Li 1s and Mg 2p would disappear and weaken after charging to 2.0 V. Figure 4f displays the ex situ XRD patterns of C-MoS_2 at different discharge/charge stages during the first cycle (marked points

https://doi.org/10.1021/acsaem.2c00611
ACS Appl. Energy Mater. 2022, 5, 6274−6281

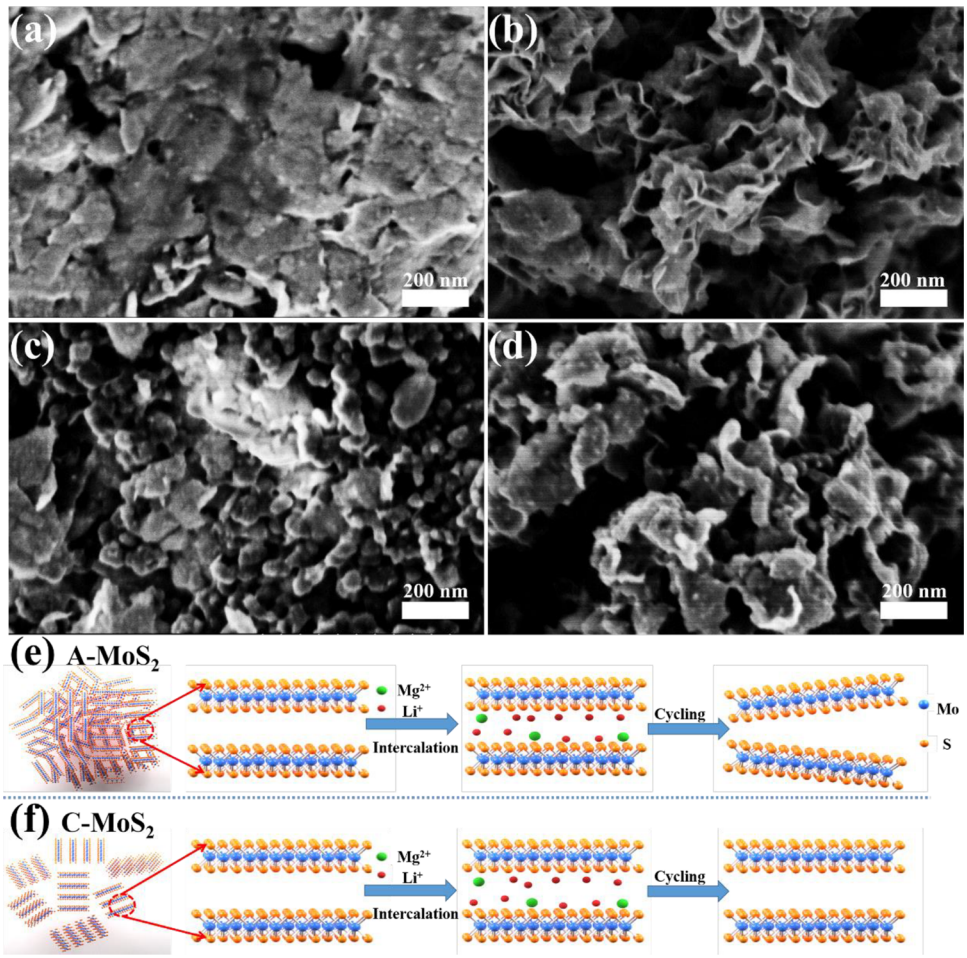

Figure 5. SEM images of A-MoS_2 and C-MoS_2 electrodes in different states. (a, b) Fresh A-MoS_2 and C-MoS_2 electrodes. (c, d) A-MoS_2 and C-MoS_2 electrodes after 50 cycles. Structure evolution scheme of (e) A-MoS_2 and (f) C-MoS_2 during the cycling process.

in Figure 4e). The pristine peak of the (002) plane for the as-prepared C-MoS_2 material is 13.65°. When discharged to 0.1 V, the characteristic peak locked at around 13.43°, which demonstrates that the (002) lattice plane gradually shifts because of the Mg^{2+}/Li^+ insertion. When charged to 2.0 V, the peak of the (002) plane would reversibly recover to 13.65° due to the Mg^{2+}/Li^+ extraction. The reversible intercalation/de-intercalation of Mg^{2+}/Li^+ is indicated by the abovementioned results. The schematic illustration of the working mechanism for MLBs is shown in Figure S10. Mg^{2+} are dissolved from the Mg anode into the electrolyte, and Mg^{2+}/Li^+ are inserted into the MoS_2 electrode during the discharging process. Because the diffusion ability of lithium ions is several orders of magnitude stronger than that of magnesium ions, the diffusion of lithium ions is very important in the intercalation process of the cathode.[44] Mg^{2+} would be deposited on the magnesium anode before lithium ions because magnesium has higher thermodynamic redox potential during the charging process.[45]

The evolution of surface morphologies for the A-MoS_2 and C-MoS_2 electrodes is observed to understand the reasons for the improvement of electrochemical stability. Figure 5a and b shows the surface morphologies of the fresh A-MoS_2 and C-MoS_2 electrodes, respectively. Figure 5c shows the morphology of fine particles for the A-MoS_2 electrode after 50 cycles, presenting that the material is crushed during the cycle process and thus exhibits very poor cyclic stability. Alternatively, the morphology of nanosheets for the C-MoS_2 electrode after 50 cycles is well maintained during the cycle process (Figure 5d) that guarantees the better cyclic stability due to its unique structure and morphology. By analyzing BET, TEM, and SEM data, it can be seen that the high dispersed nanoflowers significantly improved the structure stability of MoS_2. The bulk A-MoS_2 composed of nanosheets is not conducive to relieving the volume expansion during the cycle, thus resulting in the crushing of the structure (Figure 5e). In contrast, the highly dispersed MoS_2 nanoflowers with a large BET area and lattice spacing are more conducive to the full contact between electrolyte and material and thus sustain its structure after long-term cycling (Figure 5f). The high capacity of the C-MoS_2 derives from the large BET area and large lattice spacing, which improves the diffusion of intercalated Mg^{2+}/Li^+, and thus the material displays an improved electrochemical performance.

4. CONCLUSIONS

In conclusion, highly dispersed MoS_2 nanoflowers were successfully synthesized by using hydrochloric acid to control the concentration of sulfur ions in the solution. The obtained MoS_2 presents a unique structure with a large BET area of 118.25 $m^2\ g^{-1}$ and large lattice spacing of 0.65 nm, enabling this material to exhibit high capacity, good rate performance, and stable cycling as cathode material for hybrid Mg^{2+}/Li^+ batteries. Benefiting from the unique structure, the reversible capacity of 192.8 mA h g^{-1} over 100 cycles at 0.1 A g^{-1} was

https://doi.org/10.1021/acsaem.2c00611
ACS Appl. Energy Mater. 2022, 5, 6274−6281

obtained. The present study not only furnishes a promising cathode material for MLIBs, but also underlines a guide to fabricate highly dispersed MoS_2 materials for other applications.

■ ASSOCIATED CONTENT

Supporting Information

The Supporting Information is available free of charge at https://pubs.acs.org/doi/10.1021/acsaem.2c00611.

XPS survey spectrum, elemental mapping images, corresponding SAED pattern, rate capability, cycling performances, charge/discharge curves, equivalent circuit diagram, ex situ XPS spectra, and schematic illustration of the working mechanism for MLBs (PDF)

■ AUTHOR INFORMATION

Corresponding Authors

Baofeng Wang − *Shanghai Key Laboratory of Materials Protection and Advanced Materials in Electric Power, Shanghai University of Electric Power, Shanghai 200090, China;* orcid.org/0000-0003-2485-9509; Email: wangbaofeng@shiep.edu.cn

Xuebin Yu − *Department of Materials Science, Fudan University, Shanghai 200433, China;* orcid.org/0000-0002-4035-0991; Email: yuxuebin@fudan.edu.cn

Authors

Zhennan Xiong − *Shanghai Key Laboratory of Materials Protection and Advanced Materials in Electric Power, Shanghai University of Electric Power, Shanghai 200090, China*

Guilei Zhu − *Department of Materials Science, Fudan University, Shanghai 200433, China*

Hui Wu − *Department of Materials Science, Fudan University, Shanghai 200433, China;* orcid.org/0000-0002-0691-6349

Gejun Shi − *Shanghai Key Laboratory of Materials Protection and Advanced Materials in Electric Power, Shanghai University of Electric Power, Shanghai 200090, China;* orcid.org/0000-0001-5812-8582

Pu Xu − *Shanghai Key Laboratory of Materials Protection and Advanced Materials in Electric Power, Shanghai University of Electric Power, Shanghai 200090, China*

Huimin Yi − *Shanghai Key Laboratory of Materials Protection and Advanced Materials in Electric Power, Shanghai University of Electric Power, Shanghai 200090, China*

Yiyang Mao − *Shanghai Key Laboratory of Materials Protection and Advanced Materials in Electric Power, Shanghai University of Electric Power, Shanghai 200090, China*

Complete contact information is available at: https://pubs.acs.org/10.1021/acsaem.2c00611

Notes

The authors declare no competing financial interest.

■ ACKNOWLEDGMENTS

This work was supported by in part the National Science Fund for Distinguished Young Scholars (51625102), the National Natural Science Foundation of China (51971065 and 22075173), the Innovation Program of Shanghai Municipal Education Commission (2019-01-07-00-07-E00028), and the Technology Commission of Shanghai Municipality (No. 19DZ2271100 and 21010501100).

■ REFERENCES

(1) Yu, B.; Chen, Y.; Wang, Z.; Chen, D.; Wang, X.; Zhang, W.; He, J.; He, W. 1T-MoS_2 nanotubes wrapped with N-doped graphene as highly-efficient absorbent and electrocatalyst for Li-S batteries. *J. Power Sources* **2020**, *447*, No. 227364.

(2) Deng, Z.; Jiang, H.; Hu, Y.; Liu, Y.; Zhang, L.; Liu, H.; Li, C. 3D Ordered Macroporous MoS_2@C Nanostructure for Flexible Li-Ion Batteries. *Adv. Mater.* **2017**, *29*, No. 1603020.

(3) Tian, C.; Wu, J.; Ma, Z.; Li, B.; Zhang, X.; Zu, X.; Xiang, X.; Li, S. A melt-diffusion strategy for tunable sulfur loading on CC@MoS_2 for lithium-sulfur batteries. *Energy Rep.* **2020**, *6*, 172−180.

(4) Xu, M.; Bai, N.; Li, H.; Hu, C.; Qi, J.; Yan, X. Synthesis of MXene-supported layered MoS_2 with enhanced electrochemical performance for Mg batteries. *Chinese Chem. Lett.* **2018**, *29*, 1313−1316.

(5) Hsu, C. J.; Chou, C. Y.; Yang, C. H.; Lee, T. C.; Chang, J. K. MoS_2/graphene cathodes for reversibly storing Mg^{2+} and Mg^{2+}/Li^+ in rechargeable magnesium-anode batteries. *Chem. Commun.* **2016**, *52*, 1701−1704.

(6) Yu, X.; Zhao, G.; Liu, C.; Wu, C.; Huang, H.; He, J.; Zhang, N. A MoS_2 and Graphene Alternately Stacking van der Waals Heterostructure for Li^+/Mg^{2+} Co-Intercalation. *Adv. Funct. Mater.* **2021**, *31*, No. 2103214.

(7) Venkateswarlu, G.; Madhu, D.; Rani, J. V. Electroanalytical characterization of F-doped MoS_2 cathode material for rechargeable magnesium battery. *Funct. Mater. Lett.* **2019**, *12*, No. 1950041.

(8) Liu, Y.; Jiao, L.; Wu, Q.; Zhao, Y.; Cao, K.; Liu, H.; Wang, Y.; Yuan, H. Synthesis of rGO-supported layered MoS_2 for high-performance rechargeable Mg batteries. *Nanoscale* **2013**, *5*, 9562−9567.

(9) Sun, Y.; Chen, H.; Xing, Y.; Mao, X.; Wang, M.; Li, H.; Guo, P.; Zhao, X. S. Synthesis of MnO_2 nanowires and their capacitive behavior in aqueous electrolytes containing magnesium ions. *Colloids Surf., A* **2018**, *553*, 539−545.

(10) Liang, Y. L.; Feng, R.; Yang, S.; Ma, H. M.; Liang, J. L.; Chen, J. Rechargeable Mg Batteries with Graphene-like MoS_2 Cathode and Ultrasmall Mg Nanoparticle Anode. *Adv. Mater.* **2010**, *23*, 640−643.

(11) Zhang, Z.; Zhao, H.; Teng, Y.; Chang, X.; Xia, Q.; Li, Z.; Fang, J.; Du, Z.; Świerczek, K. Carbon-Sheathed MoS_2 Nanothorns Epitaxially Grown on CNTs: Electrochemical Application for Highly Stable and Ultrafast Lithium Storage. *Adv. Energy Mater.* **2018**, *8*, No. 1700174.

(12) Hou, X.; Shi, H.; Chang, T.; Hou, K.; Feng, L.; Suo, G.; Ye, X.; Zhang, L.; Yang, Y.; Wang, W. Hollow opening nanoflowers MoS_2-CuS-EG cathodes for high-performance hybrid Mg/Li-ion batteries. *Chem. Eng. J.* **2021**, *409*, No. 128271.

(13) Huang, H.; Zhao, G.; Zhang, N.; Sun, K. Two-dimensional Nb_2O_5 holey nanosheets prepared by a graphene sacrificial template method for high performance Mg^{2+}/Li^+ hybrid ion batteries. *Nanoscale* **2019**, *11*, 16222−16227.

(14) Cho, J. H.; Aykol, M.; Kim, S.; Ha, J. H.; Wolverton, C.; Chung, K. Y.; Kim, K. B.; Cho, B. W. Controlling the intercalation chemistry to design high-performance dual-salt hybrid rechargeable batteries. *J. Am. Chem. Soc.* **2014**, *136*, 16116−16119.

(15) Liu, C.; Zhao, G.; Zhang, L.; Lyu, P.; Yu, X.; Huang, H.; Maurin, G.; Sun, K.; Zhang, N. Self-supported PPy-encapsulated CoS_2 nanosheets anchored on the TiO_{2-x} nanorod array support by Ti-S bonds for ultra-long life hybrid Mg^{2+}/Li^+ batteries. *J. Mater. Chem. A* **2020**, *8*, 22712−22719.

(16) Wang, Y.; Wang, C.; Yi, X.; Hu, Y.; Wang, L.; Ma, L.; Zhu, G.; Chen, T.; Jin, Z. Hybrid Mg/Li-ion batteries enabled by Mg^{2+}/Li^+ co-intercalation in VS_4 nanodendrites. *Energy Storage Mater.* **2019**, *23*, 741−748.

(17) Yu, X.; Zhao, G.; Huang, H.; Liu, C.; Lyu, P.; Zhang, N. Interlayer-expanded MoS_2 nanoflowers anchored on the graphene: A high-performance Li^+/Mg^{2+} co-intercalation cathode material. *Chem. Eng. J.* **2022**, *428*, No. 131214.
(18) Vincent, M.; Avvaru, V. S.; Rodríguez, M. C.; Haranczyk, M.; Etacheri, V. High-rate and ultralong-life Mg-Li hybrid batteries based on highly pseudocapacitive dual-phase TiO_2 nanosheet cathodes. *J. Power Sources* **2021**, *506*, No. 230118.
(19) Shen, Y.; Wang, Y.; Miao, Y.; Yang, M.; Zhao, X.; Shen, X. High-Energy Interlayer-Expanded Copper Sulfide Cathode Material in Non-Corrosive Electrolyte for Rechargeable Magnesium Batteries. *Adv. Mater.* **2020**, *32*, No. 1905524.
(20) Byeon, A.; Zhao, M. Q.; Ren, C. E.; Halim, J.; Kota, S.; Urbankowski, P.; Anasori, B.; Barsoum, M. W.; Gogotsi, Y. Two-Dimensional Titanium Carbide MXene As a Cathode Material for Hybrid Magnesium/Lithium-Ion Batteries. *ACS Appl. Mater. Interfaces* **2017**, *9*, 4296−4300.
(21) Truong, Q. D.; Kempaiah Devaraju, M.; Nakayasu, Y.; Tamura, N.; Sasaki, Y.; Tomai, T.; Honma, I. Exfoliated MoS_2 and $MoSe_2$ Nanosheets by a Supercritical Fluid Process for a Hybrid Mg-Li-Ion Battery. *ACS Omega* **2017**, *2*, 2360−2367.
(22) Xu, J.; Wei, Z.; Zhang, S.; Wang, X.; Wang, Y.; He, M.; Huang, K. Hierarchical WSe_2 nanoflower as a cathode material for rechargeable Mg-ion batteries. *J. Colloid Interface Sci.* **2021**, *588*, 378−383.
(23) Tan, Y.; Zhou, F.; Huang, Z.; Yao, W.; Zhang, T.; Yao, H.; Lu, L.; Yu, S. MoS_2-Nanosheet-Decorated Carbon Nanofiber Composites Enable High-Performance Cathode Materials for Mg Batteries. *ChemElectroChem* **2018**, *5*, 996−1001.
(24) Zhang, H.; Cong, L.; Wang, J.; Wang, X.; Liu, G.; Yu, W.; Zhang, H.; Dong, X.; Fan, W. Impact of CTAB on morphology and electrochemical performance of MoS_2 nanoflowers with improved lithium storage properties. *J. Mater. Sci.: Mater. Electron.* **2018**, *29*, 3631−3639.
(25) Kun Chang, W. C.; Ma, L.; Li, H.; Li, H.; Huang, F.; Xu, Z.; Zhang, Q.; Leed, J. Y. Graphene-like MoS_2 amorphous carbon composites with high capacity and excellent stability as anode materials for lithium ion batteries. *J. Mater. Chem. A* **2011**, *21*, 6521.
(26) Fan, X.; Gaddam, R. R.; Kumar, N. A.; Zhao, X. S. A Hybrid Mg^{2+}/Li^+Battery Based on Interlayer-Expanded MoS_2/Graphene Cathode. *Adv. Energy Mater.* **2017**, *7*, No. 1700317.
(27) Liu, Y.; Fan, L.; Jiao, L. Graphene intercalated in graphene-like MoS_2: A promising cathode for rechargeable Mg batteries. *J. Power Sources* **2017**, *340*, 104−110.
(28) Novoselov, K. S.; Jiang, D.; Schedin, F.; Booth, T. J.; Khotkevich, V. V.; Morozov, S. V.; Geim, A. K. Two-dimensional atomic crystals. *Proc. Natl. Acad. Sci. U. S. A.* **2005**, *102*, 10451−10453.
(29) Yan, J.; Li, H.; Wang, K.; Jin, Q.; Lai, C.; Wang, R.; Cao, S.; Han, J.; Zhang, Z.; Su, J.; Jiang, K. Ultrahigh Phosphorus Doping of Carbon for High-Rate Sodium Ion Batteries Anode. *Adv. Energy Mater.* **2021**, *11*, No. 2003911.
(30) Mizrahi, O.; Amir, N.; Pollak, E.; Chusid, O.; Marks, V.; Gottlieb, H.; Larush, L.; Zinigrad, E.; Aurbach, D. Electrolyte Solutions with a Wide Electrochemical Window for Rechargeable Magnesium Batteries. *J. Electrochem. Soc.* **2008**, *155*, A103−A109.
(31) Sun, P.; Zhang, W.; Hu, X.; Yuan, L.; Huang, Y. Synthesis of hierarchical MoS_2 and its electrochemical performance as an anode material for lithium-ion batteries. *J. Mater. Chem. A* **2014**, *2*, 3498−3504.
(32) Göde, F.; Gümüş, C.; Zor, M. Investigations on the physical properties of the polycrystalline ZnS thin films deposited by the chemical bath deposition method. *J. Cryst. Growth* **2007**, *299*, 136−141.
(33) Najmaei, S.; Liu, Z.; Zhou, W.; Zou, X.; Shi, G.; Lei, S.; Yakobson, B. I.; Idrobo, J. C.; Ajayan, P. M.; Lou, J. Vapour phase growth and grain boundary structure of molybdenum disulphide atomic layers. *Nat. Mater.* **2013**, *12*, 754−759.
(34) Li, S.; Liu, Y.; Zhao, X.; Cui, K.; Shen, Q.; Li, P.; Qu, X.; Jiao, L. Molecular Engineering on MoS_2 Enables Large Interlayers and Unlocked Basal Planes for High-Performance Aqueous Zn-Ion Storage. *Angew. Chem. Int. Ed.* **2021**, *60*, 20286−20293.
(35) Hu, Z.; Wang, L.; Zhang, K.; Wang, J.; Cheng, F.; Tao, Z.; Chen, J. MoS_2 Nanoflowers with Expanded Interlayers as High-Performance Anodes for Sodium-Ion Batteries. *Angew. Chem. Int. Ed.* **2014**, *53*, 12794−12798.
(36) Wu, C.; Zhao, G.; Gong, S.; Zhang, N.; Sun, K. PVP incorporated MoS_2 as a Mg ion host with enhanced capacity and durability. *J. Mater. Chem. A* **2019**, *7*, 4426−4430.
(37) Wu, C.; Zhao, G.; Yu, X.; Liu, C.; Lyu, P.; Maurin, G.; Le, S.; Sun, K.; Zhang, N. MoS_2/graphene heterostructure with facilitated Mg-diffusion kinetics for high-performance rechargeable magnesium batteries. *Chem. Eng. J.* **2021**, *412*, No. 128736.
(38) Yang, W.; Han, L.; Liu, X.; Hong, L.; Wei, M. Template-free fabrication of 1D core-shell MoO_2@MoS_2/nitrogen-doped carbon nanorods for enhanced lithium/sodium-ion storage. *J. Colloid Interface Sci.* **2021**, *588*, 804−812.
(39) Ma, C.; Xu, Z.; Jiang, J.; Ma, Z.; Olsen, T.; Xiong, H.; Wang, S.; Yuan, X. Tailored nanoscale interface in a hierarchical carbon nanotube supported MoS_2@MoO_2-C electrode toward high performance sodium ion storage. *J. Mater. Chem. A* **2020**, *8*, 11011−11018.
(40) Yang, J.; Yu, L.; Zheng, B.; Li, N.; Xi, J.; Qiu, X. Carbon Microtube Textile with MoS_2 Nanosheets Grown on Both Outer and Inner Walls as Multifunctional Interlayer for Lithium-Sulfur Batteries. *Adv. Sci.* **2020**, *7*, No. 1903260.
(41) Li, Y.; Liang, Y.; Robles Hernandez, F. C.; Deog Yoo, H.; An, Q.; Yao, Y. Enhancing sodium-ion battery performance with interlayer-expanded MoS_2-PEO nanocomposites. *Nano Energy* **2015**, *15*, 453−461.
(42) Li, D.; Zhang, Y.; Sun, Q.; Zhang, S.; Wang, Z.; Liang, Z.; Si, P.; Ci, L. Hierarchically porous carbon supported Sn_4P_3 as a superior anode material for potassium-ion batteries. *Energy Storage Mater.* **2019**, *23*, 367−374.
(43) Huang, H.; Zhao, G.; Yu, X.; Shen, X.; Wang, M.; Bai, X.; Zhang, N. V-doped T-Nb_2O_5 toward high-performance Mg^{2+}/Li^+ hybrid ion batteries. *J. Mater. Chem. A* **2022**, *10*, 577−584.
(44) Li, X.; Tang, Y.; Liu, L.; Gao, Y.; Zhu, C.; NuLi, Y.; Yang, T. 2D Ti_3C_2 MXene embedded with Co(II)(OH)n nanoparticles as the cathode material for hybrid magnesium-lithium-ion batteries. *J. Mater. Sci.* **2021**, *56*, 2464−2473.
(45) Yoo, H. D.; Liang, Y.; Li, Y.; Yao, Y. High areal capacity hybrid magnesium-lithium-ion battery with 99.9% Coulombic efficiency for large-scale energy storage. *ACS Appl. Mater. Interfaces* **2015**, *7*, 7001−7007.

https://doi.org/10.1021/acsaem.2c00611
ACS Appl. Energy Mater. 2022, 5, 6274−6281